In Vivo Translation of the CIRPI System---Revealing Molecular Pathology of Rabbit Aortic Atherosclerotic Plaques

Raiyan T. Zaman*[1,2,4], Siavash Yousufi[3], Hidetoshi Chibana[4], Fumiaki Ikeno[4], Steven R. Long[5], Sanjiv S. Gambhir[6,7,8], Frederick T. Chin[6,7], Michael V. McConnell[4,7,9], Lei Xing[3,7], Alan Yeung[4]

1. Department of Radiology, Harvard Medical School
2. Gordon Center for Medical Imaging, Massachusetts General Hospital
3. Division of Medical Physics, Department of Radiation Oncology, Stanford University School of Medicine
4. Division of Cardiovascular Medicine, Department of Medicine, Stanford University School of Medicine
5. Department of Pathology, Stanford University School of Medicine
6. Department of Radiology, Stanford University School of Medicine
7. Molecular Imaging Program at Stanford University (MIPS), Stanford University School of Medicine
8. Department of Bioengineering, Stanford University Schools of Medicine and of Engineering
9. Verily Life Sciences, San Francisco, CA

*Corresponding author:
    Raiyan T. Zaman, Ph.D., MSEE
    Assistant Professor, Department of Radiology
    Harvard Medical School
    Assistant Investigator, Gordon Center for Medical Imaging
    Massachusetts General Hospital
    149, 13th Street, Charlestown, Boston, MA 02129
    Tel: (617) 643-9610 (O), (512)294-7327 (C)
    Email: rzaman@mgh.harvard.edu

Author Contributions Statement:
Specific contribution of the authors (initials) are listed here. RTZ (PI): design and system development, experimental set up and conduct experiment, data and statistical analysis, manuscript writing; SY: conduct experiment, data analysis, review and writing manuscript; HC: animal surgery and conduct *in vivo* experiment, writing manuscript; FI: helped with in vivo animal experiment and logistics; STL: histological analysis and review manuscript, SSG: provided experimental support, logistics, and manuscript review, FTC: provided FDG, and manuscript review; MVM: design and review manuscript, LX: review manuscript; AY: in vivo experimental support, and review manuscript.

Competing Interests Statement:
Michael V. McConnell is currently a Clinical Professor at the Stanford University School of Medicine and an employee of Verily Life Sciences; however, this does not alter our adherence to the *Nature Biomedical Engineering* policies on sharing data and materials.

Conflict of Interest: No potential conflicts of interest relevant to this article exist.

Data Availability Statement:
All the generated data in this study were analyzed and included in this manuscript in form of Figures and Table.

ABSTRACT

Introduction: Thin-cap fibro atheroma (TCFA) are the unstable lesions in coronary artery disease (CAD) that are prone to rupture resulting in substantial morbidity and mortality worldwide. However, their small size and complex morphological/biological features make early detection and risk assessment difficult. We tested our newly developed catheter-based **C**ircumferential-**I**ntravascular-**R**adioluminescence-**P**hotoacoustic-**I**maging (CIRPI) system in vivo to enable detection and characterization of vulnerable plaque structure and biology in rabbit abdominal aorta.

Methods: The CIRPI system includes a novel optical probe combining circumferential radioluminescence imaging (CRI) and photoacoustic tomography (PAT). The probe's CaF_2:Eu-based scintillating imaging window captures radioluminescence images (360˚ view) of plaques by detecting β-particles during ^{18}F-FDG decay. A tunable laser-based PAT characterizes tissue constituents of plaque at 7 different wavelengths—540-560 nm (calcification), 920 nm (cholesteryl ester), 1040 nm (phospholipids), 1180 nm (elastin/collagen), 1210 nm (cholesterol), and 1235 nm (triglyceride). A single B-scan is concatenated from 330 A-lines captured during a 360˚ rotation. The abdominal aorta was images in vivo in both atherosclerotic rabbits (Watanabe Heritable Hyper Lipidemic, WHHL, 13 months old male, n=5) and controls (New Zealand White, n=2). Rabbits were fasted for 6 hours before $5.55×10^7$ Bq ^{18}F-FDG was injected one hour prior to the imaging procedure. Rabbits were anesthetized and the right or left common carotid artery (CCA) was surgically exposed. A 8F catheter sheath was inserted into the CCA and a 0.014 inches guidewire was advanced to the iliac artery guided by X-ray fluoroscopy. A bare metal stent was implanted in the dorsal abdominal aorta as landmark, followed by the 7F

imaging catheters that were advanced up to the proximal stent edge (PSE). Our CIRPI and clinical OCT were performed using pullback and non-occlusive flushing techniques. After imaging with the CIRPI system, the descending aorta was flushed with contrast agent and OCT images were obtained with pull-back speed of 20 mm/sec, providing images at 100 frames/sec. Results were verified with histochemical analysis.

Results: Our CIRPI system successfully detected the locations and characterized both stable and vulnerable aortic plaques in vivo among all WHHL rabbits. Calcification was detected from the stable plaque (540/560 nm), whereas TCFA exhibited phospholipids/cholesterol (1040 nm, 1210 nm). These findings were further verified with the clinical OCT system showing an area of low attenuation filled with lipids within TCFA. PAT image illustrated broken elastic fiber/collagen that could be verified with the histochemical. All WHHL rabbits exhibited sparse to severe macrophages. Only 4 rabbits showed both moderate to severe level of calcifications and cholesterol clefts. However, all rabbits exhibited broken elastic fibers and collagen deposition. Control rabbits showed normal wall thickness with no presence of plaque tissue compositions. These findings were verified with OCT and histochemical analysis.

Conclusion: Our novel multi-modality hybrid system has been successfully translated to in vivo evaluation of atherosclerotic plaque structure and biology in a pre-clinical rabbit models. This proposed a paradigm shift that unites molecular and pathologic imaging technologies. Therefore, it may enhance the clinical evaluation of TCFA, as well as expand our understanding of CAD.

INTRODUCTION

Acute-coronary-syndrome leads to sudden reduction in perfusion and oxygenation to the myocardium resulting in heart attack. Each year, more than 20 million people with coronary artery disease (CAD) experience acute-coronary-syndrome and one-third of them die from complication(*1*).   The underlying causes of acute-coronary-syndrome are unstable lesions known as thin-cap fibro atheroma (TCFA), which are prone to rupture resulting in substantial morbidity and mortality worldwide. This is a progressive condition typically asymptotic at early stages, is characterized by the thickening of the arterial vessel wall due to the buildup of arthermanous plaque in the inner lining of the arteries (*2,3*).

Early clinical diagnosis of TCFA is thought to be critical not only to prevent catastrophic events of plaque rupture through intervention or pharmacological strategy but also contribute to the study of epidemiology of vulnerable plaques. Although, the current clinical definition of TCFA is large lipid pool, heavy infiltration of inflammatory cells/macrophages, and fibrous wall thickness <65 μm, understanding TCFA, the most common phenotype of vulnerable plaques, remains to be elucidated. For the larger-sized coronary arteries, various intravascular imaging modalities have been developed and tested clinically, including optical coherence tomography (OCT) and intravascular ultrasound (US) (*4-7*). Although, these methods provide information about the structural characteristics of the imaged vessel, they do not directly characterize biological aspects of disease (*8,9*), such as inflammation or angiogenesis (*10,11*). There is a wide range of molecular imaging modalities (such as iodinated nanoparticulate contrast agent, photoacoustic using spherical nanoparticles (*12*) and gold nanorods (*13*), IVPA with

optical contrast ([14]), MRI with wall sheer stress ([15]), CT with N1177 ([16]), PET with ^{18}F-FDG ([5]), MRI using ultra-small super-paramagnetic iron oxide probes([17,18]), SPECT using VCAM-1-specific ^{99m}Tc-labeled peptidic sequences ([19]), hybrid imaging such as simultaneous OCT for β-detection([20]), OCT-NERF system with indocyanine-green contrast agent employed for co-localization anatomical and molecular information from the artery wall. However, it is still difficult to detect TCFA in early stage due to their small size, motion, and obscuring signal from the adjacent myocardium. Therefore, an optimal intravascular imaging technology for the identification of TCFA need to possesses unique features such as visualizing endoluminal structure ([2]), identifying plaque components ([21]), providing adequate spatial resolution, and monitor plaque rupture/thrombus formation. However, due to the inherent limitations of these currently available imaging systems, an integration of multiple imaging modalities seems a synergistic solution ([22,23]).

To address these limitations we developed a multi-mode **C**ircumferential-**I**ntravascular-**R**adioluminescence-**P**hotoacoustic-**I**maging (CIRPI) system that would permit the precise location and evaluation of coronary vulnerable plaque pathology in an early stage ([24]). The goal of this feasibility study is to test the CIRPI system in *in vivo* atherosclerotic rabbit model to detect the TCFA with superior spatial resolution([25]) and improve the quantification of aortic TCFA morphology relative to other imaging modalities that are clinically available today. The innovation of this study is both technological and intellectual novelty as it aims to distinguish TCFA from stable plaques with high sensitivity/accuracy and provide quantitative image maps of TCFA with co-localized information on plaque compositions with histopathologic information([24,26]). In this study,

6

we will present the *in vivo* rabbit experiments performed with our CIRPI system to monitor disease compositions and location through mapping perturbed micro-anatomic features of TCFA.

MATERIAL AND METHODS

Circumferential Radioluminescence Imaging (CRI) Peripheral System Design

See Supplemental Methods.

Photoacoustic Tomography (PAT) Peripheral System Design

See Supplemental Methods. **Dual-Modality Endoscopic Probe**

See Supplemental Methods.

PAT Image Reconstruction

See Supplemental Methods.

Co-registered with Histological Analyses

See Supplemental Methods.

Safety Assurance

See Supplemental Methods.

Statistical Analysis

See Supplemental Methods.

Experimental Procedure of *In Vivo* Imaging of Atherosclerotic Plaque

We tested this system in *in vivo* rabbit (13 months old male, n=5, WHHL; n=2 NZW, control) abdominal aorta models according to an approved protocol by the Stanford University Administrative Panel on Laboratory Animal Care (APLAC 9948). WHHL rabbit

model is hypercholesterolemic due to a deficiency of low-density lipoprotein (LDL) receptors and has contributed to studies about lipoprotein metabolism, hypercholesterolemia, and atherosclerosis. We let the WHHL rabbits to be acclimated for seven days after arrival from the Institute for Experimental Animals, Kobe University Graduate School of Medicine (Kusunoki-cho, Chuo-ku, Kobe, Japan). Same acclimation procedure is followed for the NZW rabbits (Charles River Laboratories, USA). After seven days we have performed pre-anesthetic evaluations of rabbits by chest auscultation to determine if the rabbits are suitable candidates for imaging procedure. Once determined rabbits are fasted for 6 hours before pre-operative care was provided to them 30 minutes prior to surgery and 5.55×10^7 Bq ^{18}F-FDG was injected one hour prior to imaging.

During the procedure, rabbits were anesthetized with ketamine, xylazine, bupivacaine, and maintained with inhaled isoflurane with 3% oxygen through intubation. Hair in the neck area was shaved and 1% lidocaine was applied to vocal folds with cotton tipped applicator to facilitate intubation with endotracheal tube for maintain airways and prevent laryngospasm. A midline neck incision was made to surgically expose right or left **C**ommon **C**arotid **A**rtery (CCA, 2.85±0.15 mm in diameter) (Fig. 3B). A 8F (2.67 mm diameter) catheter sheath was inserted to CCA carefully and a 0.014 inches guidewire was advanced to CCA followed by an implantation of bare-metal stent in the dorsal abdominal aorta (4±0.38 mm diameter) as a landmark. Then a 7F (2.31 mm in diameter) imaging catheter into descending aorta guided through x-ray fluoroscopy (Fig. 3A). The CIRPI probe was needed to be within 1-3 mm of the plaques for the radioluminescence image. However, for this experiment the probe was within 0.75 µm from the arterial wall (based on acoustic signal). Our CIRPI and clinical OCT (ILUMEN™ OCT Imaging

System, Abbott, Chicago, IL, USA) were performed using pullback and non-occlusive flushing techniques. After imaging with the CIRPI system, the descending aorta was flushed with contrast agent and OCT images were obtained with pull-back speed of 20 mm/sec, providing images at 100 frames/sec. Results were verified with histochemical analysis.

RESULTS

Images from one control rabbits (ID#R817) and one WHHL (ID#R717) are shown here for discussion purpose only. The CIRPI and confirmatory clinical OCT imaging are done at the PSE located within the abdominal aorta of the control rabbit (highlighted with a green box) and they are done under the X-ray guided fluoroscopy (Fig. 1A). H&E stained (2×) histological image overviews of the tissue condition at where the CIRPI system is used to collect radioluminescene and photoacoustic images (Fig. 1B). Histology slide illustrates a normal abdominal aortic wall thickness with no atherosclerotic plaques highlighted the locations (i), (ii), (iii) and (iv) at where the CIRPI images are taken. A 360º view of the radioluminescence image and all four quadrants showed no radioluminescent signal which renders an absence of macrophages (Supplemental Fig. 4A Fig. 1C). Confirmatory clinical OCT images further validated these findings by showing normal abdominal aortic wall thickness with no atherosclerotic plaques (Fig. 1D). Highlighted (3×) section in the OCT image showed no attenuation signals, a representation of no lipids or TCFA (Fig. 1E). For the photoacoustic image no PA signals are detected at all seven tested wavelengths representing an absence of calcification, cholesterol cleft in the forms

of cholesterol ester, phospholipids, cholesterol and triglyceride, and a presence of intact elastic fibers and collagen (Fig. 1F).

The area of the abdominal aorta of a diseased WHHL rabbit that is imaged with our CIRPI system has highlighted in the x-ray fluoroscopy image (Fig. 2A). Macrophages are found within the vulnerable plaques (TCFA, wall-thickness<65 μm) located on one side of the aortic wall of the *in vivo* WHHL rabbit based on both Trichrome/H&E stained histological slides (Figs. 2B, 2C-iv, 2G). A high amount of radioluminescent signal is collected with our CIRPI probe at the location with macrophages within TCFA (Fig. 2D-iii, Supplemental Fig. 4B). Trichrome (2×) and H&E (4×) stained histological images also highlighted stable (wall-thickness>65 μm) plaques (Figs. 2B, 2C-i, ii, iv). Clinical OCT system also confirms our findings with the CIRPI system and histochemical analysis (Figs. 2E, 2F). Statistical analysis showed 203× times higher radioluminescent signal (TCFA vs. non-TCFA: $6.36×10^4±5.3×10^3$ vs. $3.14×10^1±1.91×10^1$ photon counts, p=0.003) from the area with macrophages and lipids within the TCFA compared to stable plaques (Fig. 2H).

We detected cholesterol cleft within TCFA with our CIRPI system in the forms of cholesterol ester, phospholipids, cholesterol and triglyceride upon collected PA signals at 920 nm, 1040 nm, 1210 nm, and 1235 nm wavelengths, respectively (Fig. 3C). H&E (4×) stained histological images also confirmed these tissue compositions (Figs. 3A, 3B). Further, OCT image verified these results by showing an area of low attenuation, a representation of lipid/cholesterol within the TCFA (Fig. 3D). We observed PA signals from broken elastic fibers and damaged collagens at 1180 nm wavelength with our CIRPI system (Fig. 3F). These findings were confirmed with EVG (2×) (Fig. 3E) stained

histochemical image. Calcification was detected within stable plaques when our CIRPI system laser was tuned at 540/560 nm wavelength (Fig. 3C). This finding is further confirmed with the H&E stained histological images (Figs. 3A, 3B). However, clinical OCT system is unable to detect calcification at that location. The PAT image in Fig. 3C was reconstructed from five individual PAT images representing four different lipid compositions and calcification, and then superimposed on the US image.

Overall, our CIRPI system detected sparse (n=2), moderate (n=2), and severe (n=1) macrophages in *in vivo* WHHL rabbits. Four out of five WHHL rabbits have moderate to severe calcification and severe cholesterol clefts in the forms of cholesterol ester, phospholipids, cholesterol, and triglyceride. We found 250±30.33 A.U. (p=0.001) PA signal from non-TCFA at 540/560 nm wavelength, a representation of calcification presence. However, no PA signal was detected in the TCFA for 540 nm wavelength. We observed 240±20.56 A.U. (p=0.003), 110±8.67 A.U. (p=0.004), 210±15.85 A.U. (p=0.002), and 90±5.75 A.U. (p=0.003) PA signals from lipids in the forms of cholesterol ester (920 nm), phospholipids (1040 nm), cholesterol (1210 nm), and triglyceride (1235 nm), respectively, in the area of TCFA. No PA signal was detected in the areas with non-TCFA. One of the WHHL rabbit showed early stage atherosclerosis with no calcification or cholesterol clefts. This rabbit also showed intact elastic fibers and small amount of collagen deposits. The other four WHHL rabbits exhibited broken elastic fibers and collagen deposits. Statistically, we found 80±4.71 A.U. (p=0.0001) PA signal at 1180 nm wavelength that elucidated broken elastic fibers and collagens. Clinical OCT system showed early stage atherosclerosis in two out of five WHHL rabbits with intimal hypertrophy. In addition, four out of five WHHL rabbits exhibited lipid filled TCFA with wall

thickness between 40-60 μm and they are located within 7.9-30.9 mm away from the PSE. One rabbit showed multiple TCFAs along with several stable plaques. Histology analysis corroborated these findings by showing occlusion between 10%-60%. Control rabbits showed normal abdominal aortic wall thickness with no plaques using our CIRPI system and verified with the clinical OCT system and histological analysis. Results from each rabbit is shown in Supplemental Table 1.

DISCUSSION

We have demonstrated that our multi-modality catheter-based CIRPI system can detect ^{18}F-FDG uptake by the macrophages within the TCFA of *in vivo* rabbit abdominal aorta with high resolution and sensitivity and is capable of simultaneously characterizing plaque morphologic compositions. These findings were verified with clinical OCT and ultrasound imaging systems, as well as immunohistochemical analyses of the molecular composition and pathologic status. The data based on radioluminescence and photoacoustic signals illustrated low variability based on the statistical analysis. The radioluminescence signal variability among all disease rabbits are between 8.33%. Based on the photoacoustic signals the disease tissue compositions showed variabilities between 5.89-12.13% (calcification: 12.13%, cholesterol ester: 8.56%, phospholipids: 7.88%, cholesterol: 7.54%, triglyceride: 6.38%, and elastin/collagen: 5.89%). The lowest variability was observed among elastin/collagen whereas calcification varied the most. We were not able to discuss these results in ratio as we found no PA signal for calcification (540/560 nm) from TCFA and cholesterol ester, phospholipids, cholesterol, triglyceride, and broken elastic fibers/collagen from non-TCFA.

Our integrated CIRPI system offers an unprecedented opportunity for intravascular detection and characterization of the biology and morphology of atherosclerotic plaques that provides a multiparametric analysis of pathognomonic constituents of vulnerable plaques. This approach will both broaden our understanding about human CAD and enable prognostic data for this deadly disease. Such measurements have important implications for guiding treatment that may ultimately lead to reduce the risk of heart attack and the debilitating aftermath.

Based on the results analysis, we found if the aortic occlusion is less than 10%, the plaques are mostly early stage with moderate macrophages. Also, it has no calcification or cholesterol clefts, and its elastic fibers are still intact with small amount of collagen deposition. When the aortic occlusion is between 25%-60%, we identified severe macrophages, calcifications, and cholesterol clefts in the form of cholesterol ester, phospholipids, cholesterol, and triglyceride located over 500 μm to 1 mm area. In some rabbits, multiple TCFAs and stable plaques were identified in close vicinity. Most of these severe atherosclerotic abdominal aortas of the WHHL rabbits revealed broken elastic fiber and collagen deposition. The endogenous chromophores calcification, lipids cause the enhanced signal to background ratios.

Our CIRPI system employs intravascular molecular imaging approach by utilizing optical, photoacoustic imaging in conjunction with ^{18}F-FDG. The system collected radioluminescent and PA signals to detect the exact location of TCFA and demonstrated its usefulness for disease characterization through biological imaging of atherosclerotic plaques. Based on this feasibility study we demonstrated that our multi-modality CIRPI prototype system was sufficiently sensitive towards the detection of ^{18}F-FDG in *in vivo*

TCFA with good resolution. Thus, our novel system in conjunction with radionuclide molecular probes may lead to intravascular imaging platforms for coronary arterial molecular imaging in clinic.

Coronary imaging remains challenging with PET or other currently available imaging modalities due to small size, constant motion, and in the case of ^{18}F-FDG, obscuring uptake by adjacent myocardium (*27*). Although ^{18}F-FDG uptake is a marker for viable myocardium, this myocardial uptake makes it harder to image the adjacent small-sized coronaries (*28*), though there are some promising initial results (*29*). This makes an intravascular imaging approach advantageous, minimizing the distance and maximizing the sensitivity to coronary plaque signal. While PET ^{18}F-FDG has been well studied, there are other PET agents being investigated, such as ^{18}F-labeled mannose (*30*), which could also be studied in future by our CIRPI system.

As any scintillating screen with a thickness as small as 1 mm provides an intrinsic efficiency close to 10% due to annihilation photons, we chose to use a scintillating screen made of CaF_2:Eu with a thickness of 0.150 mm. Due to this extremely thin screen, the CIRPI system eliminates a significant amount of annihilation photons, which would have come from distant tissues such as bladder caused by high γ-radiation from urine or γ-contamination that is spill in from myocardium and hinder the imaging of the local ^{18}F-FDG uptake in the plaque. Also, this thin scintillating imaging window let small fraction of energy deposition from the γ-particles due to Compton interaction. Therefore, it was unlikely that the γ-particles would have interacted with the scintillator to create background noise. Thus, subtraction of the γ-radiation signal was not considered. We

used a typical radiation dose, despite the nature of this feasibility study of the CIRPI system for in vivo imaging.

In this study, we have developed the central hypothesis on detecting and characterizing lipid-rich plaques using our CIRPI system through sufficiently well differentiated absorption spectra of lipids from those of the constituents of normal arterial tissue in the 740 to 1400 nm wavelength range. Although, we observed cholesterol clefts in the forms of cholesterol ester, phospholipid, cholesterol, and triglyceride in in vivo rabbit abdominal aorta with our CIRPI system, we could not confirm the presence of individual components of lipids with the histochemical analysis and clinical OCT system (histology and OCT cannot distinguish specific lipid components). However, we were able to correlate large lipid pools at the TCFA with both histology and the clinical OCT system. Thus, downscaling photoacoustic imaging of the CIRPI system provides a tool for understanding metabolic pathways. Because hypermetabolism is a quintessential hallmark of TCFA atherosclerotic plaques, metabolic photoacoustic may enable clinical CAD screening at the earliest stage without using exogenous contrast agents.

We found that our design of the CIRPI system is suitable for early detection/characterization of vulnerable plaque with high sensitivity/accuracy and to track the plaque biology/morphology by multiparametric analysis of pathognomonic compositions of TCFA. Several intravascular hybrid imaging systems including IVIS-Xray, OCT-Xray, IVUS-CTCA, OCT-CTCA, NIRS-IVUS, IVUS-OCT, OCT-NIRF, IVUS-NIRF, OCT-NIRS, IVUS-IVPA, and IVUS-FLIM were developed over the years to detect and evaluate atherosclerotic plaques. These systems were evaluated based on their ability to get information on lumen dimension, plaque burden, positive remodeling, lipid content,

and cap thickness. These hybrid imaging systems mentioned here have the ability to perform three of these areas efficiently unlike our CIRPI system which can perform all five. In these hybrid systems NIRS-IVUS (3-16 mm), IVUS-OCT (1 mm), OCT-NIRF (1-3 mm), OCT-NIRS (1.5 mm), and IVUS-IVPA (4-5 mm) are considered the best with respect to mm range resolution. However, none of the imaging systems have the resolution in μm as our CIRPI system (1.2 μm). Acquisition time varies among all hybrid systems specially IVIS-OCT (20-45 sec/image), OCT-NIRF (44 ms/image), and OCT-NIRS (2.5-4 min/image). These three hybrid systems have the best acquisition time compared to other hybrid imaging systems mentioned here. Our CIRPI system has the acquisition time of 2 min/image. Thus, the acquisition time of our CIRPI system is comparable with the top three intravascular hybrid imaging systems that are discussed in this manuscript.

It is important to evaluate our CIRPI system sensitivity with respect to other intravascular β-detecting scintillator-based (BC-408 plastic) imaging systems such as intravascular radiation detector (IVRD)(*31*). However, it is almost impossible to compare the CIRPI system to other imaging modalities a this is the first time that CaF_2:Eu phosphor was ever used to make an imaging window for catheter-based system. In addition, IVRD was used to collect β-particles from 115, 230, and 1,335 kBq ^{18}F-FDG point fixed-sources in the femoral artery of a dog instead of IV injection. The IVRD probe consists of only 100 optical fibers that can only create spectral images unlike our CIRPI system that has 18,000 optical image fibers to create a 360º image of the artery.

We found that our design of the CIRPI system is suitable for early detection/characterization of vulnerable plaque with high sensitivity/accuracy and to track the plaque biology/morphology by multiparametric analysis of pathognomonic

compositions of TCFA. This approach can both broaden our understanding about human CAD and enable prognostic data for this deadly disease. Therefore, such measurements will have important implications for guiding treatment that may ultimately lead to reduce the risk of MI and the aftermath. Thus, this CIRPI system may propose a paradigm shift in the diagnosis and risk stratification of CAD. The synergy that would be created by this imaging system could unite molecular and pathologic information associated with TCFA. Therefore, our CIRPI system with advanced catheter design can reveal molecular aspects of plaque pathobiology that may constitute a valuable and indispensable ally in this challenging quest.

The CIRPI system catheter probe needs to be within 1-3 mm of a vulnerable plaques to capture signal from the beta-particle emitting from ^{18}F-FDG decay despite the FOV of 6.5 mm. This close distance between the plaques and probe may increase the risk of rupturing TCFA. Another limitation to the system is the probes rigid scanning heat as it limited the bending radius of the probe. In future, we plan to reduce the length of the rigid head with decrease the radius.

Despite these limitations with the current CIRPI system, we demonstrate future potential for clinical detection, diagnosis, and treatment of human coronary atherosclerosis and offer the possibilities for expanding our understanding of CAD. The CIRPI system was designed with essential features that will enable intravascular imaging for clinical characterization of vulnerable coronary plaques and is destined to have an impact on how we manage this disease.

CONCLUSIONS

Although significant advancements have been done in medical imaging, CAD remains the number one cause of death in the United States and worldwide. Early detection of atherosclerosis and prevention of myocardial infarction and sudden cardiac death have remained critical unmet medical needs, which we address using this multimodality imaging approach. Last fifteen years molecular imaging strategies have become an integral part of basic science and recently in clinical diagnosis of numerous disease. However, there remains a substantial translational gap for molecular imaging of coronary atherosclerosis in patients. Our multimodality molecular tissue imaging approach comprised of an integrated fiber-optic CIRPI system, harnessing light, radioluminescence, and sound to detect and characterize vulnerable atherosclerotic plaques. We could outline the plaque location with characteristic information pertaining to specific tissue compositions. Our catheter-based system provides the high sensitivity and resolution needed for coronary plaque imaging. Radioluminescence and photoacoustic imaging are ripe for clinical translation, particularly as there are multiple FDA-approved radionuclides (e.g., ^{18}F-FDG). We demonstrated the potential for clinical detection and evaluation of both in vivo vulnerable and non-vulnerable atherosclerotic plaques via CIRPI, plus the potential for expanding our understanding of CAD to ultimately improve how we manage this disease.

REFERENCES

1.   Go AS, Mozaffarian D, Roger VL, et al. Executive summary: heart disease and stroke statistics--2014 update: a report from the American Heart Association. *Circulation.* 2014;129:399-410.

2.   Ross R. The pathogenesis of atherosclerosis: a perspective for the 1990s. *Nature.* 1993;362:801-809.

3.   Ross R. Atherosclerosis--an inflammatory disease. *N Engl J Med.* 1999;340:115-126.

4.   Garcia-Garcia HM, Costa MA, Serruys PW. Imaging of coronary atherosclerosis: intravascular ultrasound. *Eur Heart J.* 2010;31:2456-2469.

5.   Chen IY, Wu JC. Cardiovascular molecular imaging: focus on clinical translation. *Circulation.* 2011;123:425-443.

6.   Jang IK, Tearney GJ, MacNeill B, et al. In vivo characterization of coronary atherosclerotic plaque by use of optical coherence tomography. *Circulation.* 2005;111:1551-1555.

7.   Yabushita H, Bouma BE, Houser SL, et al. Characterization of human atherosclerosis by optical coherence tomography. *Circulation.* 2002;106:1640-1645.

8.   Calfon MA, Vinegoni C, Ntziachristos V, Jaffer FA. Intravascular near-infrared fluorescence molecular imaging of atherosclerosis: toward coronary arterial visualization of biologically high-risk plaques. *J Biomed Opt.* 2010;15:011107.

9.   Kim JW, Jaffer FA. Emerging Molecular Targets for Intravascular Imaging of High-Risk Plaques. *Current Cardiovascular Imaging Reports.* 2010;3:237-247.

10.   Sanz J, Fayad ZA. Imaging of atherosclerotic cardiovascular disease. *Nature.* 2008;451:953-957.

11.   Jaffer FA, Libby P, Weissleder R. Molecular imaging of cardiovascular disease. *Circulation.* 2007;116:1052-1061.

12. Wang B, Yantsen E, Larson T, et al. Plasmonic intravascular photoacoustic imaging for detection of macrophages in atherosclerotic plaques. *Nano Lett.* 2009;9:2212-2217.

13. Yeager D, Karpiouk A, Wang B, et al. Intravascular photoacoustic imaging of exogenously labeled atherosclerotic plaque through luminal blood. *J Biomed Opt.* 2012;17:106016.

14. KRISTA JANSEN GVS, ANTONIUS F. W. VAN DER STEEN. INTRAVASCULAR PHOTOACOUSTIC IMAGING: A NEW TOOL FOR VULNERABLE PLAQUE IDENTIFICATION. *Ultrasound in Medicine and Biology.* 2014;40:12.

15. Groen HC, Gijsen FJ, van der Lugt A, et al. Plaque rupture in the carotid artery is localized at the high shear stress region: a case report. *Stroke.* 2007;38:2379-2381.

16. Hyafil F, Cornily JC, Feig JE, et al. Noninvasive detection of macrophages using a nanoparticulate contrast agent for computed tomography. *Nat Med.* 2007;13:636-641.

17. McLachlan SJ, Morris MR, Lucas MA, et al. Phase I clinical evaluation of a new iron oxide MR contrast agent. *J Magn Reson Imaging.* 1994;4:301-307.

18. Tang TY, Howarth SP, Miller SR, et al. The ATHEROMA (Atorvastatin Therapy: Effects on Reduction of Macrophage Activity) Study. Evaluation using ultrasmall superparamagnetic iron oxide-enhanced magnetic resonance imaging in carotid disease. *J Am Coll Cardiol.* 2009;53:2039-2050.

19. Dimastromatteo J, Broisat A, Perret P, et al. In Vivo Molecular Imaging of Atherosclerotic Lesions in ApoE-/- Mice Using VCAM-1-Specific, 99mTc-Labeled Peptidic Sequences. *J Nucl Med.* 2013.

20. Zhu Q, Piao D, Sadeghi MM, Sinusas AJ. Simultaneous optical coherence tomography imaging and beta particle detection. *Opt Lett.* 2003;28:1704-1706.

21. Moreno PR. Vulnerable plaque: definition, diagnosis, and treatment. *Cardiol Clin.* 2010;28:1-30.

22. Bourantas CV KI, Plissiti ME, et al. A method for 3D reconstruction of coronary arteries using biplane angiography and intravascular ultrasound images. *Comput Med Imaging Graph.* 2005;29:597– 606.

23. Garcia-Garcia HM, Gonzalo N, Granada JF, Regar E, Serruys PW. Diagnosis and treatment of coronary vulnerable plaques. *Expert Rev Cardiovasc Ther.* 2008;6:209-222.

24. Zaman RT, Yousefi S, Long SR, et al. A Dual-Modality Hybrid Imaging System Harnesses Radioluminescence and Sound to Reveal Molecular Pathology of Atherosclerotic Plaques. *Sci Rep.* 2018;8:8992.

25. Zaman RT, Kosuge H, Carpenter C, Sun C, McConnell MV, Xing L. Scintillating balloon-enabled fiber-optic system for radionuclide imaging of atherosclerotic plaques. *J Nucl Med.* 2015;56:771-777.

26. Zaman R, *et al.* Harnessing Radioluminescence and Sound to Reveal Molecular Pathology of Atherosclerotic Plaques. *J Nucl Med* 2017;58.

27. Gaeta C, Fernandez Y, Pavia J, et al. Reduced myocardial 18F-FDG uptake after calcium channel blocker administration. Initial observation for a potential new method to improve plaque detection. *Eur J Nucl Med Mol Imaging.* 2011;38:2018-2024.

28. Inglese E, Leva L, Matheoud R, et al. Spatial and Temporal Heterogeneity of Regional Myocardial Uptake in Patients Without Heart Disease Under Fasting Conditions on Repeated Whole-Body 18F-FDG PET/CT. *Journal of Nuclear Medicine.* 2007;48:1662-1669.

29. Rogers IS, Nasir K, Figueroa AL, et al. Feasibility of FDG imaging of the coronary arteries: comparison between acute coronary syndrome and stable angina. *JACC Cardiovasc Imaging.* 2010;3:388-397.

30. Tahara N, Mukherjee J, de Haas HJ, et al. 2-deoxy-2-[18F]fluoro-D-mannose positron emission tomography imaging in atherosclerosis. *Nat Med.* 2014;20:215-219.

31. Hosokawa R, Kambara N, Ohba M, et al. A catheter-based intravascular radiation detector of vulnerable plaques. *J Nucl Med.* 2006;47:863-867.
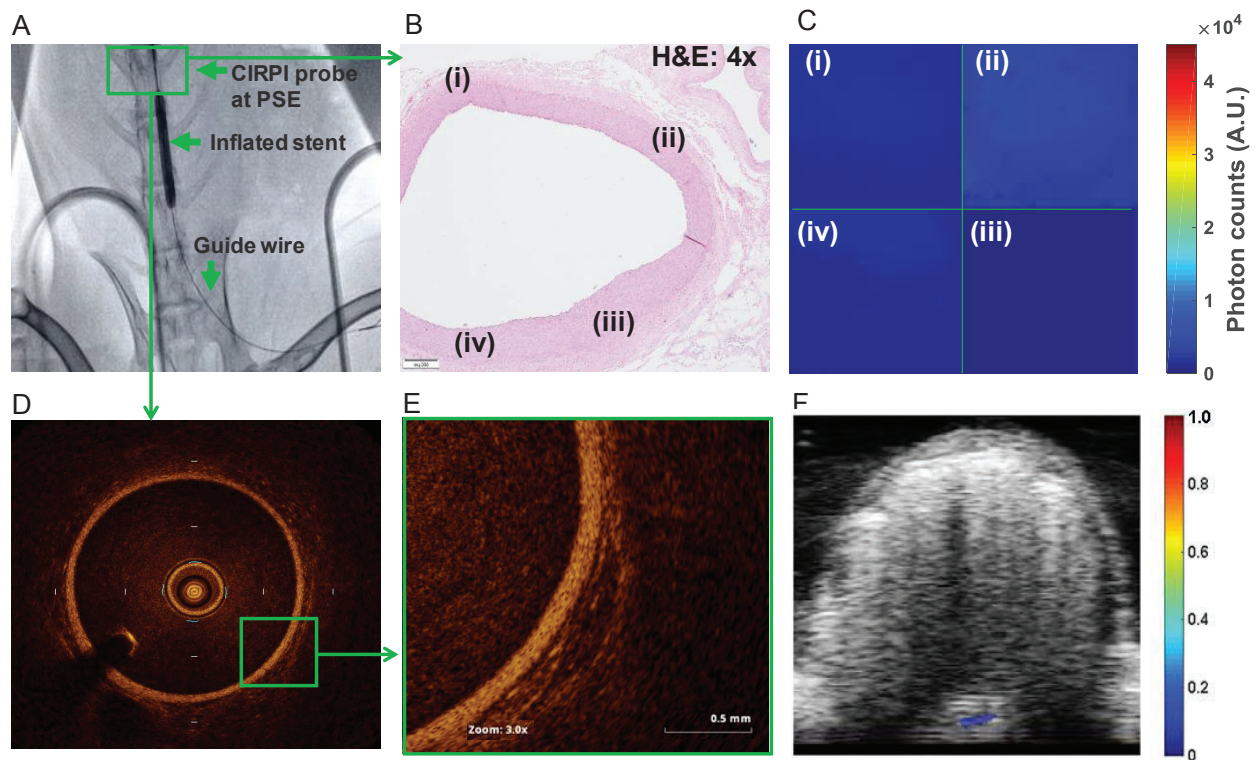
Fig 1. In vivo abdominal aorta images of the control rabbit. (A) X-ray guided fluoroscopy image illustrated that a guide wire is followed by the CIRPI probe located at the peripheral stent edge (PSE is used as a land mark). (B) H&E stained (2×) histological image overviews the tissue condition at where the CIRPI system is used to collect radioluminescene and photoacoustic images. Further the same location was imaged with a clinical OCT system for secondary verification. Histology slide illustrated a normal abdominal aortic wall thickness with no atherosclerotic plaques. (C) Radioluminescence images are collected at every 1.43° with the scanning probe. Each quadrant (i), (ii), (iii), and (iv) is the representation of the concatenated images between starting point of the scan up to 90°. Each quadrant of the radioluminescence image represented the precise location of the histological slide that are highlighted with the same number. None of the quadrant of the radioluminescence image showed radioluminescent signal that renders an absence of macrophages. (D) Confirmatory OCT images further validated these findings by showing normal abdominal aortic wall thickness with no atherosclerotic plaques. (E) Highlighted section in the OCT image showed no attenuation signals, a representation of no lipids or TCFA. (F) In the photoacoustic image no PA signals are detected at all seven tested wavelengths representing an absence of calcification, cholesterol cleft in the form of cholesterol ester, phospholipids, cholesterol and triglyceride, and a presence of intact elastic fibers and collagen.
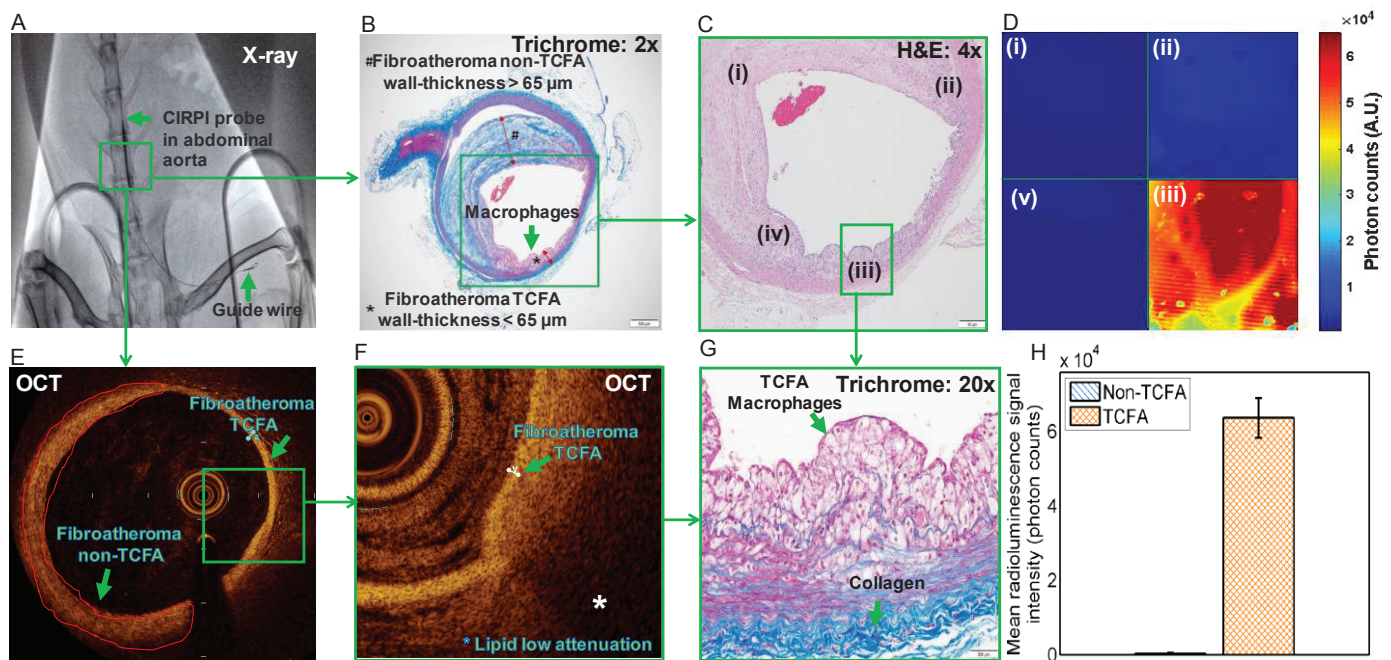
Fig 2. In vivo images of the abdominal aorta with atherosclerotic plaques in WHHL rabbit. (A) X-ray guided fluoroscopy image illustrated the CIRP probe followed by guide wire marked with stent (highlighted within a green box). Histological images are presented to give the overview of the plaque orientation within the CRI imaging area using our CIRPI system and secondary verification with a clinical OCT system. (B) Trichrome stained (2×) abdominal aorta highlighted the stable plaque, fibroatheroma non-TCFA with wall thickness > 65 µm. On the opposite wall there was a clear evidence of fibroatheroma TCFA with a wall thickness < 65 µm filled with macrophages. (C) H&E stained (4×) abdominal aorta showed four highlighted locations (i), (ii), (iii) and (iv) in the histology image that are the same location of each quadrant of the CIRPI image; (i), (ii), and (iii) represent non-TCFA, and (iv) TCFA with large macrophage accumulation. (D) Radioluminescence images are collected at every 1.43º with the scanning probe. Each quadrant is the representation of the concatenated images between starting point of the scan up to 90º. Each quadrant of the radioluminescence image represented the precise location of the histological slide that are highlighted with the same number. The quadrant four of the radioluminescence image exhibited high radioluminescent signal that is the indicative of large number of macrophage accumulation within the TCFA (E) Confirmatory OCT images validated the presence of non-TCFA and TCFA at the arterial wall of the abdominal aorta. (F) Highlighted section in the OCT image showed low attenuation signal, a representation of lipids within TCFA. (G) Trichrome stained TCFA area illustrated large number of macrophages that represents the same area with lipids in the OCT image. (H) Statistical analysis showed 203× higher radioluminescent signal (TCFA vs. non-TCFA: $6.36\times10^4\pm5.3\times10^3$ vs. $3.14\times10^1\pm1.91\times10^1$ photon counts, p=0.003) from the area with macrophages and lipids within TCFA compared to non-TCFA.
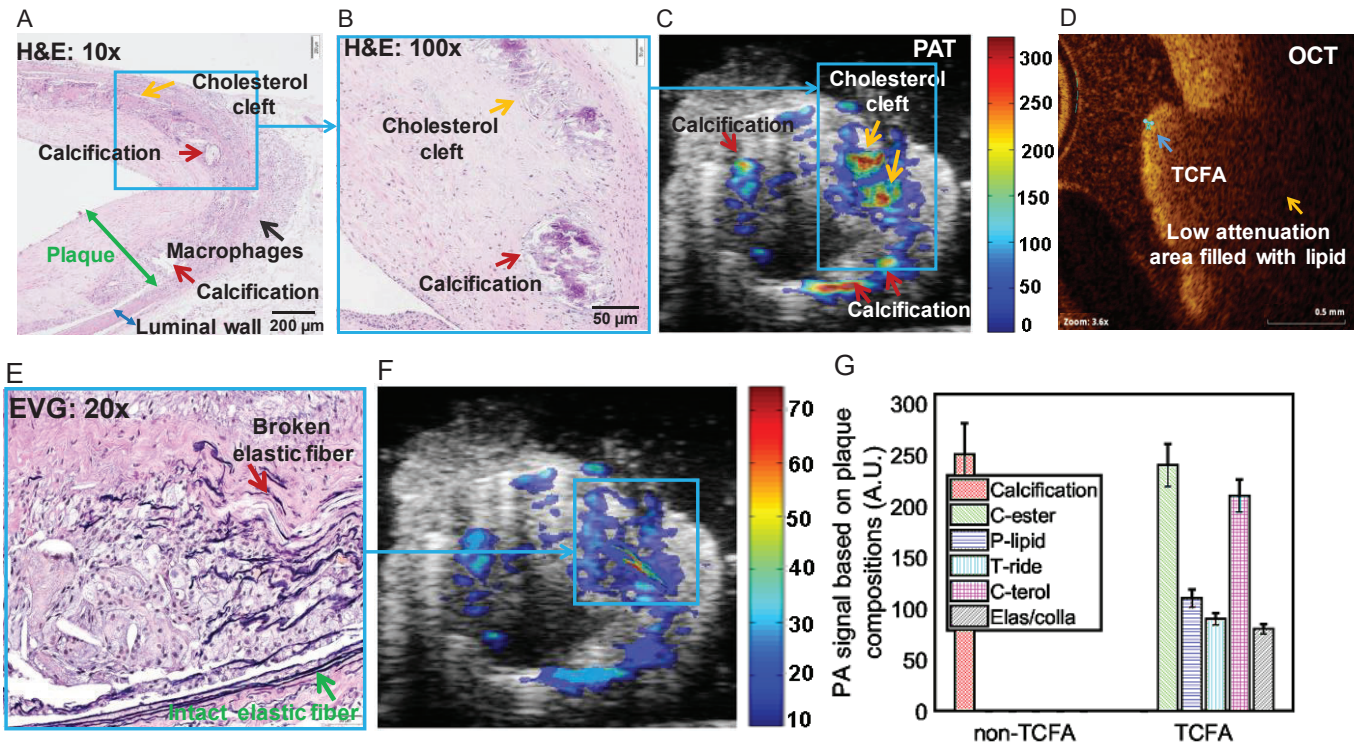
Fig 3. Images of in vivo atherosclerotic plaques in rabbit abdominal aorta. (A) Histological images are presented to give the overview of the plaque orientation within the PAT imaging area using our CIRPI system and secondary verification with a clinical OCT system. H&E stained (10×) abdominal aorta highlighted plaques containing trace amount of calcification and prominent cholesterol cleft/lipids in close vicinity to macrophages, fibroatheroma TCFA with wall thickness<65 µm. (B) Enlarged image of (A) showed severe cholesterol cleft and trace amount of calcification. (C) In PAT image high PA signals were detected at the area with cholesterol, calcification. (D) Confirmatory OCT images validated the presence of presence of lipids at the arterial wall of the abdominal aorta. Highlighted section in the OCT image showed low attenuation signal, a representation of lipids within TCFA. (E) EVG (20×) stained area illustrated both broken (red arrow) and intact collagen (green arrow). (F) High PA signal was detected at the area with broken collagen in the PAT image collected with the CIRPI system. (G) Statistical analysis showed high PA signal from (i) non-TCFA calcification (250±30.33, p=0.001, no other signal was observed); (ii) TCFA: cholesterol ester (240±20.56, p=0.003), phospholipids (110±8.67, p=0.004), cholesterol (210±15.85, p=0.002), and triglyceride (90±5.75, p=0.003), which represent the presence of severe lipids; elastin/collagen (80±4.71, p=0.0001) that elucidates broken/damage elastic fibers and collagen.

SUPPLEMENTAL MATERIALS AND METHODS

Circumferential Radioluminescence Imaging (CRI) Peripheral System Design

The components of CIRPI system is described in our previously published study[26]. In brief, the optical components of the CIRPI system consists of a 10x magnification infinity-corrected microscope objective (RMS10x, Olympus Inc.) with a working distance of 10.6 mm, numerical aperture (NA) of 0.25 and effective focal length (EFL) of 18 mm (Supplemental Fig. 1). The system also contains an infinity-corrected tube lens for plan fluorite objective (ITL200, Thorlabs) in between the objective (F2 = 102 mm) and the ProEM charge-coupled device (CCD) camera (F3 = 200 mm) (Princeton Instruments). The CIRPI system provides a 360˚ view inside an artery through an innovative probe design (see section on Dual-Modality Endoscopic Probe).

The novelty of this CIRPI system is based on a scintillating window made from organic calcium fluoride doped with europium (CaF_2:Eu) phosphor, placed on the catheter-based probe to convert the β-particles of the positron emission signal into visible light due to radioactive decay (primary decay time 940 ns). The molecules in the scintillating window get excited with the incoming ionizing radiation, especially β-particles from the decay of ^{18}F-FDG, or other isotopes, by absorbing energy. When these molecules return to a lower energy state from an excited state, they release optical radiation in the visible range. This light is then captured with a *highly sensitive* CCD camera using deep thermoelectric cooling at -70°C for minimizing the background signal from the temperature-dependent dark current, hot pixel blemishes, and vibration. The deep thermoelectric cooling was done with a CoolCUBE II liquid circulatory system. The camera exposure times were set to 45 seconds based on sensitivity (above this threshold the pixels were saturated). For ^{18}F-FDG imaging with the CIRPI system, the binning factor was set at smallest limit (1x1 pixel) with effective active imaging resolutions of 1024 x

1024 pixels (width x height). The analog-to-digital conversion speed was set to 10 MHz with corresponding EM gain of 50 at 16-bits bit depth. The storage shift rate was set to 600 ns with readout time of 4 ms for 'frame transfer' readout mode. The CCD camera shutter mode was set to "always open" without any delay (0 ms) in opening and closing. The selection process of optimal scintillating material and resolution were described in the our previously published manuscript [25].

Photoacoustic Tomography (PAT) Peripheral System Design

The PAT peripheral system has re-designed to perform faster data acquisition from our previously published study.[24] For PAT system, we used a tunable Horizon I OPO pumped by Surelite II nanosecond laser (192-2750 nm Continiuum, San Jose, CA, USA) with 4-7 mm beam diameter (before focusing into the 200 µm core multimode fiber). The peak wavelength of the laser's spectral bandwidth can be tuned to multiple values for selective imaging of the different tissue constituents. The central hypothesis of this PAT imaging is that the absorption spectra of calcium, lipids, elastic, and collagen are sufficiently well differentiated from those of the constituents of normal arterial tissue in the 500 to 1400 nm wavelength range to permit the detection of calcium or lipid-rich plaques using PAT imaging.

The repetition rate was set to the highest at 20 Hz with 3-5 ns FWHM pulse length. The laser was linearly polarized at <2 mrad divergence. The Horizon tunable laser operates at 110 V and is connected to Surelite 210. Power supply for Surelite 210 operates at 220 V and attached to a coolant circulation to regulate the temperature. Horizon sends an Sync Out signal as an external trigger to a pulse-receiver signal generator (5073PR-15U, 75 MHz Bandwidth, 39dB, RF Gain, 115 VAC Olympus America Inc., Waltham, MA, USA). A pre-amplifier receives the PA signal from the multi-mode

optical probe and after 8× amplification this signal is sent to pulser-receiver. This 75 MHz computer controlled pulser-receiver is used to trigger a four-channel, 14-bit Digital Acquisition System (NI PXIe-5170R, 250 MS/s, 100 MHz, Oscilloscope with 750 MB RAM and Kintex-7 325T FPGA, NI, USA) and receive the amplified PA signal. A custom written Matlab code was used to concatenate 330 A-lines captured during a 360˚ rotation to generate a B-scan.

Dual-Modality Endoscopic Probe

The components of CIRPI system probe is described in our previously published study[26]. However, the probe is reduced in diameter. The CIRPI system includes a novel optical probe combining circumferential radioluminescence imaging (CRI) and photoacoustic tomography (PAT) (Supplemental Fig. 2A). The probe's CaF_2:Eu-based scintillating imaging window captures radioluminescence images (360˚ view) of plaques by converting β-particles to visible photons during ^{18}F-FDG decay (Supplemental Fig. 2B). A single 360º arterial radioluminescence image acquisition is 45 seconds for our CIRPI system. During radioluminescence imaging, the visible photons from optical radiation of high energy β-particles reflect to/from the 45º scanning mirror. These photons were then collected through the GRIN lens followed by creating a 18,000 pixels image at every 1.43º rotation of the mirror. A total of 63 images were collected for each quadrant of the circular arterial wall. A tunable laser-based PAT characterizes tissue constituents of plaque at 7 different wavelengths—540-560 nm (calcification), 920 nm (cholesteryl ester), 1040 nm (phospholipids), 1180 nm (elastin/collagen), 1210 nm (cholesterol), and 1235 nm (triglyceride) (Supplemental Fig. 2C).

The CIRPI probe (Supplemental Figs. 2D, 2E) has a 840 mm flexible tether with up to 17˚ of bending freedom and a 36 mm (previously 42 mm) long rigid distal imaging

head consists of (1) a CaF$_2$:Eu scintillating imaging window, (2) a light guiding multi-mode optical fiber (OF-1, 0.22 NA, 0.2 mm core diameter; Thorlabs Inc., USA), (3) a leached image fiber (OF-2, 18,000 optical fibers represent a 0.9 mm diameter imaging area with 7.4 μm pixel size; Schott Inc., USA), (4) a single-element ultrasonic transducer (Lithium Niobate LNO, 40 MHz, unfocused, ring transducer with OD = 2 mm, ID = 1.37 mm, and length of 5.1 mm), (5) a digital actuator (2.0 mm diameter, 18.62 mm long; Namiki Precision Jewel Co., Ltd. Japan), and (6) 45° degree flat rotating mirror (2 mm diameter, protected aluminum on glass substrate, with the reflection surface at 45° to the probe's axis; Edmund Optics Inc., USA) that was placed in a stainless steel tube housing. The absolute field-of-view of 0.9 mm imaging area is 6.5 mm. A single-element ultrasonic transducer was used for achieving a high Signal to Noise Ratio (SNR) at MHz repetition rates. Laser pulses from a portable UV-VIS-NIR tunable laser (7 ns pulse length at 20 Hz repetition rate) were coupled into a multimode fiber using a 10x microscope objective. These laser pulses are guided by the multi-mode optical fiber which is also positioned parallel to an imaging fiber-bundle belonging to the CIRPI system. These pulses are then emitted into the tissue through a central hole (1.37 mm diameter) in the transducer located in the distal end of the probe. The distal end of the OF-2 was terminated by a 1 mm diameter Gradient-Index (GRIN) lens designed to have a working distance of 5 mm, and paraxial magnification of 5.86. The GRIN lens provides an NA of 0.5, and radial index gradient has a maximum central refractive index of 1.635 at the lens axis.

The scintillating window was fabricated from a polymer based polyvinyl toluene block made of CaF$_2$:Eu phosphor (Saint-Gobain Crystals, Hiram, OH, USA). CaF$_2$:Eu was selected as the optimal scintillating materials with respect to highest radioluminescent signal[25]. The phosphor has a refractive index of 1.58 with 68% light output. The scintillating efficiency was 10,400 photons/1 MeV e-. It has a maximum emission at 435

4

nm wavelength with a temporal pulse width of 2.2 ns (FWHM). The scintillating window was machined into a cylindrically shaped tube with 10 mm length and wall thickness of 0.150 mm. The outer diameter (OD) and inner diameter (ID) of the window is 2.31 mm and 2.01 mm, respectively. Radioluminescence is produced within the scintillating imaging window following the emission of a beta particle from a radiotracer (^{18}F-FDG) within a macrophage. The optical photons were captured by a high-numerical-aperture 10x microscope objective coupled to a deep-cooled ProEM CCD camera. This scintillating window can detect radioluminescent signal from the disease tissue within the travel distance of β-particles (1-3 mm in tissue) emitted from the ^{18}F-FDG decay. The CRI peripheral system provides the overall spatial resolution of the CIRPI system that is 1.2 µm based on our previous study[25]. Spatial resolution of the CRI was calculated based on modulation transfer function (MTF). MTF is an important aid to objective evaluation of the image-forming capability of our CRI peripheral system, providing a means of expressing the imaging quality of the optical system objectively and quantitatively, plus predicting performance reliably. The detection limit and overall radioluminescence signal sensitivity of our system was identified to be 10,020 (photon counts) based on a 1 µCi closed disk β-source.

Circumferential sector scanning (B-scan) was accomplished by rotating a 45° flat mirror. The mirror was driven by a geared actuator (gear ratio, 254:1) to steer the laser beam from the optical fiber to the tissue and the acoustic wave from the tissue to the ultrasonic transducer (UST). A single 360° arterial PAT image acquisition time is 1.15 seconds for our CIRPI system. Therefore, the overall detection speed for a 360° view of an artery with our CIRPI system took only few minutes (≈2 minutes). When the pulsed laser light illuminated atherosclerotic plaque, the optical absorbers there (such as lipid, cholesterol, calcification) undergo thermo elastic expansion, generating an acoustic

pressure wave which was detected with the UST. The mirror was also important for reflecting visible light to the OF-2 due to the vibration of molecules within the scintillating imaging window upon the deposition of β-particles energy from the ^{18}F-FDG decay. As water and glass have a large ratio of sound propagation speeds, the scanning mirror has exhibited total external reflection within the acceptance angles of the ultrasonic transducer and the GRIN lens, and thus, contributed to no additional propagation losses into the ultrasonic and visible light detection. The scanning mirror system had enabled circumferential B-scanning without moving other illumination optics and the ultrasonic sensor. The optical fibers, the transducer's signal wires, and the actuator wires were encapsulated in a flexible catheter body with outer diameter of 2.31 mm where 0.5 mm was used for a catheter enclosure. The mirror's rotational speed was kept constant, while providing a matching medium for acoustic wave propagation, the transducer and scanning mirror's housing space was water-coupled with deionized water through a 0.25 mm hole on the 0.180 mm thick scintillating imaging window. The actuator was isolated from the water with a spacer, and the torque was required for the mirror rotation that is transferred through a micro-magnetic (OD 1.58 mm with a length of 3.175 mm, K&J Magnets Inc., USA) coupling mechanism.

PAT Image Reconstruction

PAT images are created from the generation of thermoelastic stress waves by heating endogenous chromophores (e.g., calcification, cholesterol) or exogenous contrast agents in an optically heterogenous medium with a short laser pulse. These stress waves contain information about the distribution of structures with preferential optical absorption. Therefore, information about the relative concentrations of endogenous chromophores or exogenous contrast agents can be determined allowing

enhanced signal to background ratios. The low optical absorption and US scattering of disease tissues makes it optimal for PAT imaging at high resolution and depth (maximum 3-5 cm deep). However, for this study we adjusted the depth to be between 5-8 mm.

The temporarily confined optical absorption induces a temperature rise ΔT and consequently an initial pressure rise p_0 due to thermoelastic expansion: $p_0 = \beta . \Delta T/k$, where k is the isothermal compressibility. The PA signal was collected every 1.43° rotating step of the scanning mirror for photoacoustic acquisition at seven different wavelengths. The PAT image was developed one laser pulse per image line. The procedure of PA signal processing includes high-pass signal filtering, compensation for acoustic diffraction, detection of the irradiated surface position and rejection of the reverberating signal. Radial back-projection algorithm for image reconstruction was developed and included in the Labview/Matlab computer code. Laser induced noise was removed with singular value decomposition method.

Co-Registered with Histological Analyses and OCT

After the in vivo imaging experiments, WHHL (n=5) and NZW (n=2) rabbit dorsal abdominal aortic samples were cut from the distal edge of the stent (used as a landmark) and placed in 10% formalin, and submitted for paraffin embedding, sectioning, and staining. Step sections (5 µm thick, n=16) were collected at different levels beginning at the proximal end of the stent to exclude the aorta containing stent (otherwise blade would brake) and proceeding to the other end. The sections were mounted on glass microscopic slides, stained with hemotoxylin and eosin, trichrome (collagen), and EVG (elastin) reagents and covered with Tissue Tek Film as cover slips.

The microscopic slides were examined with an Olympus BX51 microscope fitted with diffuse white light (LM) and transmission polarizing (TPM) optics and 2x, 4x, 10x,

20x, and 40x objectives. Selected fields were imaged by pathologist at Stanford SOM using Zeiss Axiocam MRc5 digital camera mounted on the microscope and Zeiss AxioVision SE64 Rel 4.8 software supported by a Dell Optiplex 980 Desktop Computer. The histological study was based on a quantitative analysis of disease tissue constituents that were co-register with the CIRPI results and clinical OCT based on the stent location.

Safety Assurance

After each experiment, we used classical gamma counting analog meter, Geiger-Muller counter, to perform safety assurance on the instruments, counter top, whole body, and lab coat, that there was no contamination from ^{18}F-FDG. Each time the count per minute was around 30-50 CPM that was in normal range of 0.03-0.05 mR/hr.

Statistical Analysis

A pairwise two-sample Student's t-test was performed to compare *in vivo* radioluminescent signal intensity from the ^{18}F-FDG-enriched vulnerable plaques and stable plaques. The same t-test was performed for PA signals as well for both TCFA and non-TCFA. As WHHL rabbits had similar weight (5±0.02lb) and same dose, these factors were not considered in the statistical analysis. Therefore, weight and dose were eliminated during the statistical process. Rabbit samples were not randomized. These analyses were performed using custom written MATLAB code. We presented all values as mean ± standard deviation. We considered P<0.05 as statistically significant for all ex vivo analyses.

For a significance level of P<0.05 and a statistical power of 0.90, each group should comprise of at least N=5 animals to obtain a statistically significant result. We used an equation for sample size calculation for a study comparing two means:

$N=\{4*\sigma^2(Z_{crit}+Z_{pwr})^2\}/ D^2$ where N is sample size, D is the minimum expected CNR difference based on the means of the two groups (plaque vs. control), σ is assumed standard deviation of each group (assumed to be equal for both group) be 1.65, $Z_{crit} =$ 1.960 for significance level of 0.05(95) (standard normal deviate corresponding to selected significance criteria) and $Z_{pwr} = 1.645$ for statistical power of 0.95 (standard normal deviate corresponding to selected statistical powers) .

Table 1. Observations of In Vivo Rabbit Samples with CIRPI, OCT, and Histochemical Analysis

Species	Observation		
Rabbit ID	CIRPI Image Analysis	OCT Image Analysis	Histochemical Analysis
# R317 Gender: Male Age: 13 months (Disease WHHL rabbit)	1. Moderate macrophages 2. No calcification 3. No cholesterol clefts in the forms of cholesterol ester, phospholipids, cholesterol, and triglyceride 4. Presence of intact elastic fibers and collagen	1. Only intimal hypertrophy 2. Early stage atherosclerosis 3. No lipid filled TCFA plaques 4. Early stage plaques are developing 17.1 mm away from proximal stent edge (PSE)	1. 10% or less occlusion 2. Near the PSE showed macrophage accumulation and thrombus 3. No mineralized calcium 4. No lipid/cholesterol 5. 500 µm plaque area 6. Small amounts of collagen deposition and presence of intact elastic fiber
# R417 Gender: Male Age: 13 months (Disease WHHL rabbit)	1. Moderate macrophages 2. Moderate calcification 3. Presence of severe cholesterol cleft in forms of cholesterol ester, phospholipids, cholesterol, and triglyceride 4. Presence of broken elastic fibers and collagen	1. TCFA (wall thickness 65 µm) starts from 7.9 mm from PSE 2. Continuous plaques in the entire length of the vessel wall 3. One side of the vessel wall is normal thickness while the other end of the wall is developing plaques with Narrowing of the vessel diameter	1. 30% lumen occlusion 2. Moderate macrophages 3. Moderate mineralized calcium 4. Moderate cholesterol and lipid deposition 5. Moderate inflammation 6. 600 µm plaque area 7. Presence of broken elastic fibers and collagen
# R517 Gender: Male Age: 13 months (Disease WHHL rabbit)	1. Sparse macrophages 2. Moderate calcification 3. Severe cholesterol clefts in forms of cholesterol ester, phospholipids, cholesterol, and triglyceride 4. Presence of broken elastic fibers and collagen	1. TCFA started from 14.1 mm away from PSE 2. Lipid filled plaques with 40 µm wall thickness 3. Most stable plaques were between the PSE and TCFA	1. 25% lumen occlusion 2. Moderate macrophages 3. Moderate mineralized calcium 4. Severe lipid/giant cells with moderate cholesterol formation 5. Moderate chronic inflammation 6. 750 µm plaque area 7. Presence of broken elastic fibers and collagen
# R617 Gender: Male Age: 13 months (Disease WHHL rabbit)	1. Severe macrophages 2. Severe calcification 3. Severe cholesterol ester, phospholipids, cholesterol, and triglyceride 4. Presence of broken elastic fibers and collagen	1. Intimal hypertrophy 2. Both TCFA and stable plaques are present 3. Presence of multiple TCFA and stable plaques • 1st TCFA: 40 µm wall thickness (10 mm away from the PSE) • 2nd TCFA (at the end): 50 µm wall thickness (14.7 mm away from PSE) • Stable plaque: 180 µm wall thickness) (32.8 mm away from PSE)	1. 60% lumen occlusion 2. Severe macrophages 3. Severe mineralized calcium 4. Minimal inflammation 5. Severe cholesterol clefts and lipid deposition 6. 500 µm plaque area 7. Presence of broken elastic fibers and collagen

# R717 Gender: Male Age: 13 months (Disease WHHL rabbit)	1. Sparse macrophages 2. Severe calcification 3. Severe cholesterol ester, phospholipids, cholesterol, and triglyceride 4. Presence of broken elastic fibers and collagen	1. Intimal hypertrophy 2. Mostly early stage atherosclerosis with few TCFA and stable plaques 3. TCFA with a wall thickness of 60 µm is located 30.9 mm away from PSE 4. Mostly stable plaques from PSE up to 30.9 mm where the TCFA started	1. 45% lumen occlusion 2. Sparse macrophages 3. Severe mineralized calcium 1. 500 µm plaque area with 1 mm length 2. Calcification 3. Macrophages or histocytes 4. Cholesterol cleft 5. Broken elastic fiber
# R817/R917 Gender: Male Age: 13 months (Control NZW rabbit)	1. No macrophages 2. No calcification 3. No cholesterol cleft 4. Presence of intact elastic fibers and collagen	1. No atherosclerotic plaques 2. Normal wall thickness	1. No evidence of atherosclerotic plaques, calcification, cholesterol, or macrophages 2. Normal wall thickness 3. Presence of intact elastic fibers and collagen
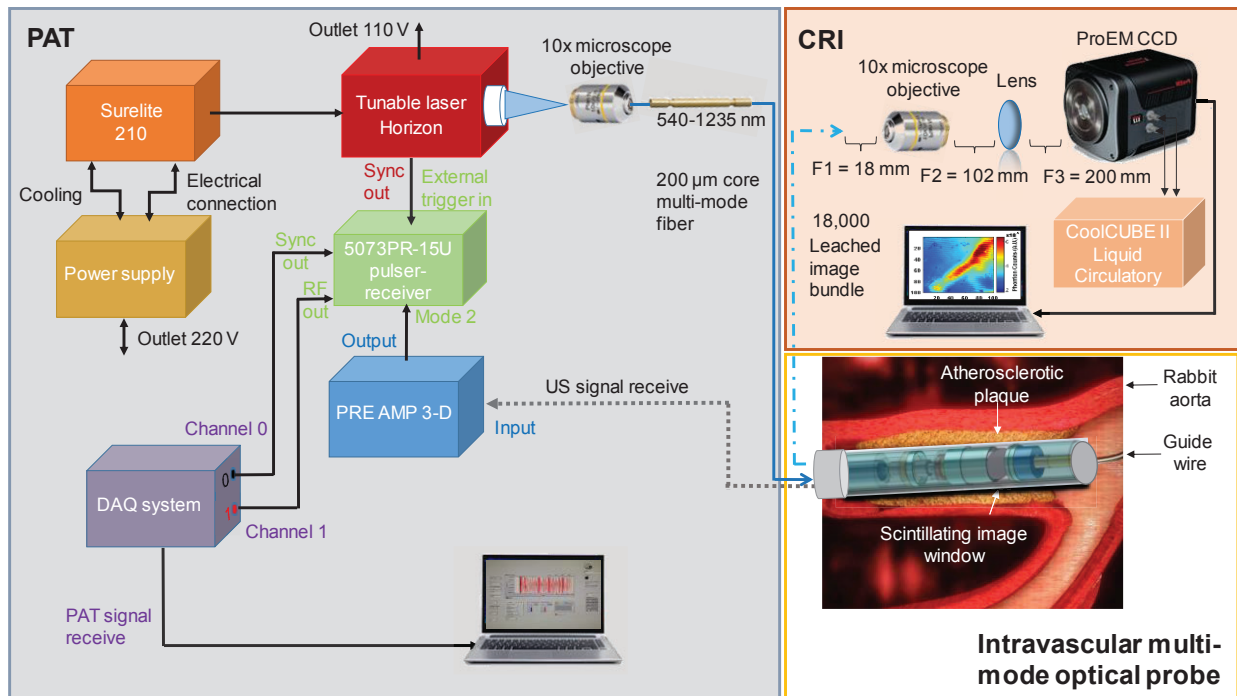
Supplemental Fig 1. Schematic diagram of the dual-modality CIRPI system for detection and characterization of atherosclerotic plaque. The CIRPI system has three main components (1) CRI, detects and outlines the location of vulnerable plaque by identifying macrophage accumulations, (2) PAT, characterize the plaque by disease tissue compositions, and (3) multi-mode optical probe that collects radioluminescent and PA signals. CRI peripheral system consists of (1) a 10x magnification infinity-corrected microscope objective (2) an infinity-corrected tube lens for plan fluoride objective in between the objective (F2 = 102 mm) and the ProEM charge-coupled device (CCD) camera (F3 = 200 mm). PAT system consists of (1) tunable laser, (2) pulser-receiver, (3) pre-amplifier, (4) data acquisition board (DAQ system).

A B C

D E
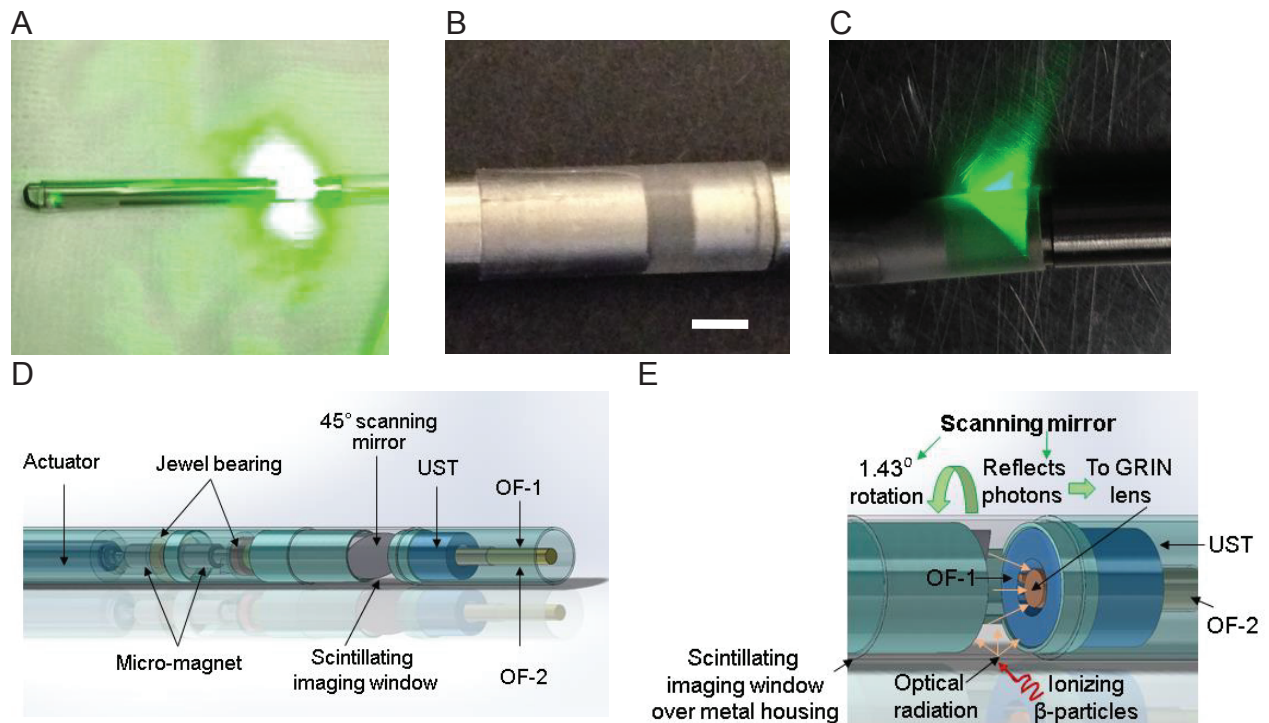
Supplemental Fig 2. Photograph of the (A) multi-mode optical probe with scintillating imaging window (B) scintillating imaging window is made from CaF_2:Eu phosphor (scale bar: 1 mm) that converts beta particles to visible photons, (C) tunable laser light is delivered through water coupled scintillating window at 540 nm (Visible, green), 560 nm (Visible, green), and 1040 nm wavelength (NIR, Near InfraRed). Schematic diagram of the CIRPI (D) probe design shows the main components (1) CaF_2:Eu scintillating imaging window, (2) OF-1: 0.2 mm core multimode light guiding optical fiber, (3) OF-2: 18K pixels imaging fiber, (4) UST: single element unfocused ultrasonic transducer, (5) digital actuator, and (6) 45° degree flat rotating mirror, (E) optical pathway of the visible photons reflecting from the scanning mirror to the GRIN lens at every 1.43° rotation and facilitating a single radioluminescence image with 18,000 pixels through OF-2.

A

B
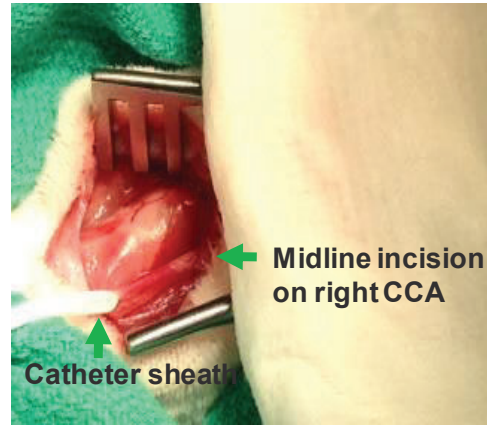
Supplemental Fig 3. In vivo rabbit expertient is conducted in a surgical suite. (A) Interventional cardiologist is inserting the imaging catheter with a guide wire through a midline incision on either the right/left CCA guiding through a X-ray fluoroscopy. (B) A catheter sheath is inserted throught a midline incision on the right CCA after the tissue was separted and hold with a speculum.
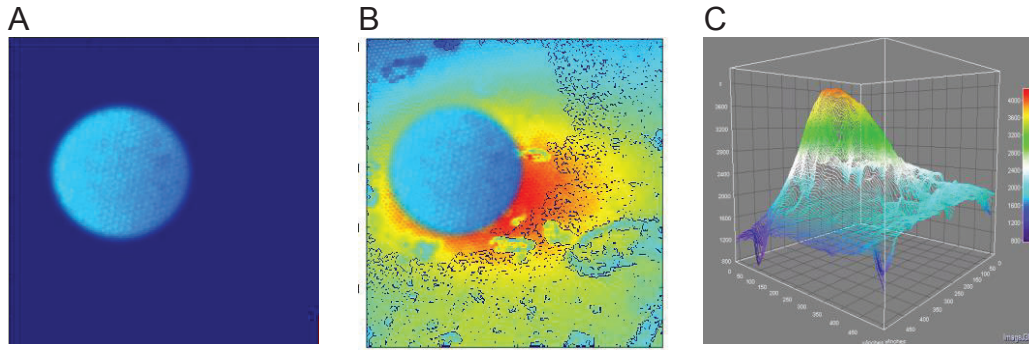
Supplemental Fig 4. A reconstructed radioluminescence image of a 360º arterial view (A) control rabbit, (B) disease rabbit. (C) Contour plot of the diseased rabbit.